

# Granular Impact: A Grain-scale Approach

Abram Clark,<sup>1</sup> Alec Petersen,<sup>1</sup> Lou Kondic,<sup>2</sup> Corey O'Hern,<sup>3</sup> and R.P. Behringer<sup>1</sup>

<sup>1</sup>*Department of Physics & Center for Non-linear and Complex Systems,  
Duke University, Science Drive, Durham NC 27708-0305, USA*

<sup>2</sup>*Department of Mathematics, New Jersey Institute of Technology, Newark USA*

<sup>3</sup>*Department of Mechanical Engineering, Yale University, New Haven, USA*

(Dated: February 19, 2022)

This work summarizes a series of studies on two-dimensional granular impact, where an intruding object strikes a granular material at high speed. Many previous studies on granular impact have used a macroscopic force law, which is dominated by an inertial drag term proportional to the intruder velocity squared. The primary focus here is on the microscopic force response of the granular material, and how the grain-scale effects give rise to this inertial drag term. We show that the inertial drag arises from intermittent collisions with force-chain-like structures. We construct a simple collisional model to explain the inertial drag, as well as off-axis instability and rotations. Finally, we show how the granular response changes when the intruder speed approaches  $d/t_c$ , leading to a failure of the inertial drag description in this regime. Here,  $d$  is the mean particle diameter and  $t_c$  the characteristic momentum-transfer time between two grains.

PACS numbers: 83.80.Fg, 62.20.D-, 83.85.Vb

Keywords: Granular Materials, Impact, Force Networks

## INTRODUCTION

The physics of an intruding object impacting and penetrating a granular material is relevant to many situations, including soil penetration, meteor impacts, and ballistics. Related phenomena occur in industrial settings, for instance in mixers or other machinery, where a blade can impact a material. There is a large relevant literature, of which we note a number of references, including the references which they cite [1–17]

During an impact, a number of coupled processes are at work, and most of these are only partially understood. At the largest scale, the granular material exerts a force on the intruder, bringing it to rest. The momentum and kinetic energy of the intruder are transferred into the grains at the interface of the intruder and granular material, and then carried deeper into the material. The time and space scales that are relevant for these transfers must be determined to understand the drag force on the intruder.

A useful macroscopic starting point is a group of often-used empirical models for the force experienced by the intruder. Here, we base our discussion on a typical model (see also previous work [1, 3–6, 8–10]) with the form:

$$F = m\ddot{z} = mg - f(z) - h(z)\dot{z}^2. \quad (1)$$

$F$  is the force on the intruder,  $z$  is the depth within the material, where  $z = 0$  corresponds to the point where the lower edge of the intruder first touches the granular surface,  $mg$  is the gravitational force,  $f(z)$  is a static term,  $h(z)$  characterizes the strength of the inertial ( $\dot{z}^2$ ) term, and dots denote time derivatives. Often,  $h(z)$  is assumed to be constant, though we find that it can have an initial transient. The static term,  $f(z)$  is often assumed linear in  $z$ . Although such models are empirical, they typically capture the ‘slow’ dynamics (i.e., neglecting short-time fluctuations) of intruder trajectories. However, it is important to understand the grain scale origins of these terms.

This equation is often dated back to Poncelet in the 1800s, and we will refer to it as the Poncelet model [18]. We understand it qualitatively in terms of three forces which act on the intruder: gravity, a static elastic or pressure-related force, and a collisional or momentum transfer term, which should be proportional to the square of the intruder speed,  $\dot{z} = v$ . The last point follows from the collisional nature of the impact. During the majority of a typical impact, the collisional (third) term dominates. But, when the intruder comes to rest, the static term is important. This equation has been tested in various settings, where it frequently provides a good description of the motion of the intruder [1, 4–6, 8–10].

However, Eq. 1 contains only the most basic physics, and at this point, there is no direct connection to the particle properties (such as the stiffness of the grains, their size relative to the intruder, their shape) or to properties of the intruder (such as its mass or shape). What are the grain-scale physical processes which give rise to this equation? When and why might it break down? In the discussion below, we show that the Poncelet equation works well to describe the slowest time scales of the intruder dynamics in a series of two-dimensional impact experiments into granular systems comprised of photoelastic disks. We provide a deeper understanding of the origin of the collisional

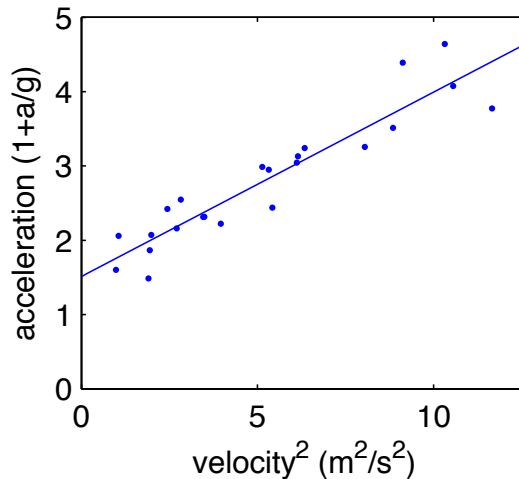


FIG. 1: Plot of  $a$  versus  $v^2$  for a circular intruder at a fixed depth,  $z = \zeta$ , where each data point represents one trajectory with varying initial velocities. The slope and offset of a linear fit to this data yield  $f(\zeta)$  and  $h(\zeta)$ . However, large acceleration fluctuations make precise extraction of these values difficult without simplifying assumptions, e.g.,  $h(z) = b = \text{constant}$ , where  $b$  is the average  $h(z)$  for all depths. See Ref. [9] for more details.

term, proportional to  $\dot{z}^2$ , in terms of our grain-scale observations. Additionally, we look at how the microscopic physics changes when the impact speed approaches the speed at which forces propagate within the material, and we show how and why the Poncelet model breaks down. Further insight into this regime of fast impact is reached by discrete element simulations.

### TESTING THE FORM OF THE PONCELET EQUATION

Testing the Poncelet equation requires data for the acceleration of the intruder. Such data has been obtained and successfully fitted to a Poncelet-like model in a few cases [4, 5, 8, 9], almost always in a regime where the intruder speed is much smaller than a typical force propagation speed within the granular material. Here, we consider data by Clark et al. [8, 9] for circular intruders impacting beds of photoelastic particles from above. More details are given in the experimental methods section, and for the moment, we note that the results of this subsection pertain to initial intruder speeds of up to 6 m/s onto the hardest of the three types of particles which we have studied [8–10]. The impact speed in this set of experiments is much less than the granular force transmission speed (typically, in these materials, forces propagate at roughly  $v_f \approx 300$  m/s), and measurements of the acceleration of the intruder are made on a time scale (after filtering) of  $\sim 10^{-2}$  s. On this time scale, there are significant fluctuations of the intruder acceleration, but it is still possible to obtain a ‘slow time’ measure of the intruder speed and acceleration as a function of depth below the point of impact. The depth-dependent coefficients  $f(z)$  and  $h(z)$  can be determined from a plot of the intruder acceleration,  $a$  plotted as a function of  $v^2$ . To obtain this plot, we made multiple repetitions at different impact speeds in order to map out the depth dependence of  $f$  and  $h$ . Fig. 1 gives an example for a circular intruder.

As written, the Poncelet equation is a nonlinear second order equation in  $z(t)$ . However, by recasting this equation using the identity  $m\ddot{z} = dK/dz$ , familiar from basic mechanics, it becomes (e.g. Eq. 2) a first order linear equation for  $K(z)$ , the kinetic energy, as a function of depth, with non-constant coefficients. it is then possible to write a formally exact solution for  $K(z)$ .

$$\frac{dK}{dz} = mg - f(z) - \frac{2h(z)}{m}K. \quad (2)$$

Once  $K(z)$  is determined by integrating Eq. 2,  $z(t)$  follows by writing  $\dot{z} = (2K(z)/m)^{1/2}$ , integrating  $t(z) = \int_0^z dz (2K(z)/m)^{-1/2}$ , and inverting. If the forms of  $f(z)$  and  $h(z)$  are simple, the calculation can be done explicitly. For example, using the commonly assumed forms  $f(z) = f_0 + kz$  and  $h(z) = b$ , we obtain  $K(z)$  as

$$K(z) = (K_0 - c_1) \exp(-c_2 z) + c_1 - c_3 z. \quad (3)$$

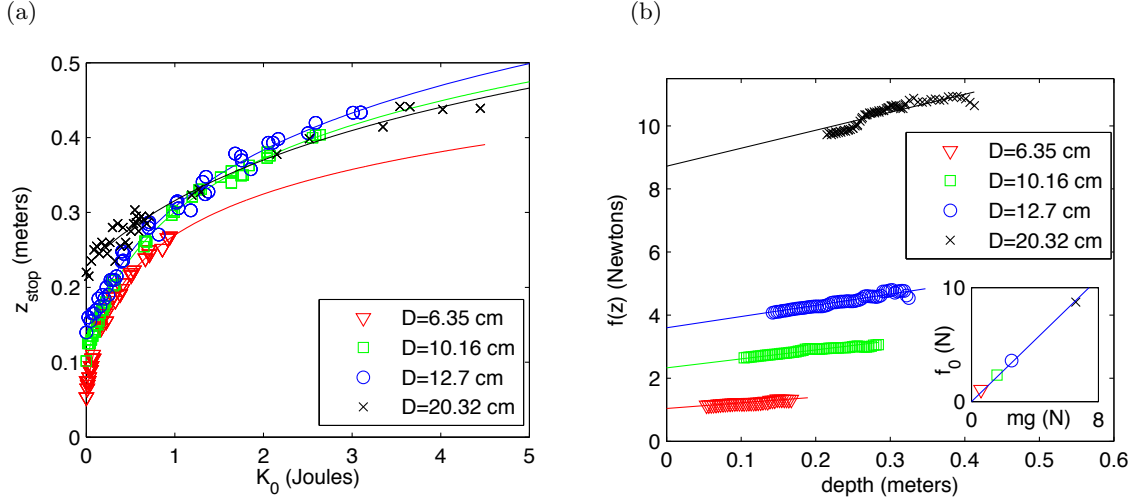


FIG. 2: (a) Plot of  $z_{stop}$  vs.  $K_0$ , with fits of the form  $a \log(bK_0 + 1) + c$ . (b) Plot of  $f(z)$  for circular intruders. Linear fits are  $f_0 + kz$ , where the slope,  $k$ , corresponds to hydrostatic pressure. Inset shows plot of  $f_0$  vs.  $mg$ , with a linear fit through the origin, with slope 1.35.

Here, the constants are  $c_1 = [(mg - f_0)c_2 + k]/c_2^2$ ,  $c_2 = 2b/m$ , and  $c_3 = k/c_2 = km/(2b)$ .

Even without integrating, it is possible to find the stopping distance by setting  $K(z_{stop}) = 0$ , which yields the stopping depth as a function of impact energy,  $K_0$ . For the common case described by Eq. 3, the stopping depth,  $z_{stop}$ , varies as the log of  $K_0$ :

$$z_{stop} = \frac{m}{2b} \log \left[ \frac{\frac{2b}{m} K_0 + (f_0 + \frac{km}{2b}) - mg}{(f_0 + kz_{stop} + \frac{km}{2b}) - mg} \right]. \quad (4)$$

If  $f(z)$  as roughly constant,  $f(z) = f_0$  and  $k = 0$ , then the form for the stopping distance is simpler. In this case,  $z_{stop}$  still increases logarithmically with  $K_0$ , as in [2, 3, 5].

$$z_{stop} = \frac{m}{2b} \log \left[ 1 + \frac{2b}{m} \left( \frac{K_0}{f_0 - mg} \right) \right]. \quad (5)$$

Such an approximation is increasingly relevant as the intruder speed increases, and the  $\dot{z}^2$  term dominates.

Recasting the Poncelet equation in terms of kinetic energy is also advantageous in fitting experimental data to the Poncelet equation, since only velocity data is needed, and not acceleration data. For further discussion on this, see [9]. In Fig. 2(b), and Fig. 3, we show data for  $h$  and  $f(z)$ , fitted using the kinetic energy approach. The static term  $f(z)$  is a linear function of  $z$  to a good approximation. The drag coefficient,  $h(z)$ , is nearly constant after an initial transient near the free granular surface, and we show the average drag coefficient,  $h_0$ , as a function of intruder size and shape in and Fig. 3.

## A GRAIN-SCALE FORCE PICTURE

The collisional term, involving the coefficient  $h(z)$  is the dominant drag term for much of the duration of a collision. What are the grain-scale physical processes which give rise to this term? Figure 4 shows a series of photoelastic images, taken from a high-speed movie of an impact, where bright particles are experiencing a strong force. These images suggest a qualitative picture for the case we are studying: in the regime where the Poncelet equation is valid and the intruder speed is well below the granular force propagation speed, the intruder excites forces along filamentary structures, that are similar in nature to the force chains of static or quasi-static deformations of granular materials [19–25]. However, unlike in the static case, forces propagate dynamically along the filamentary force network. The network structure evolves in time as the intruder plows through the material, but it is relatively long-lived compared to the time for a signal to propagate along a segment of the network.

The forces carried by the force network fluctuate at high frequencies, as suggested by the images shown in Fig. 4. An immediate question is, do the fluctuations in the photoelastic signal really correspond to fluctuations that are

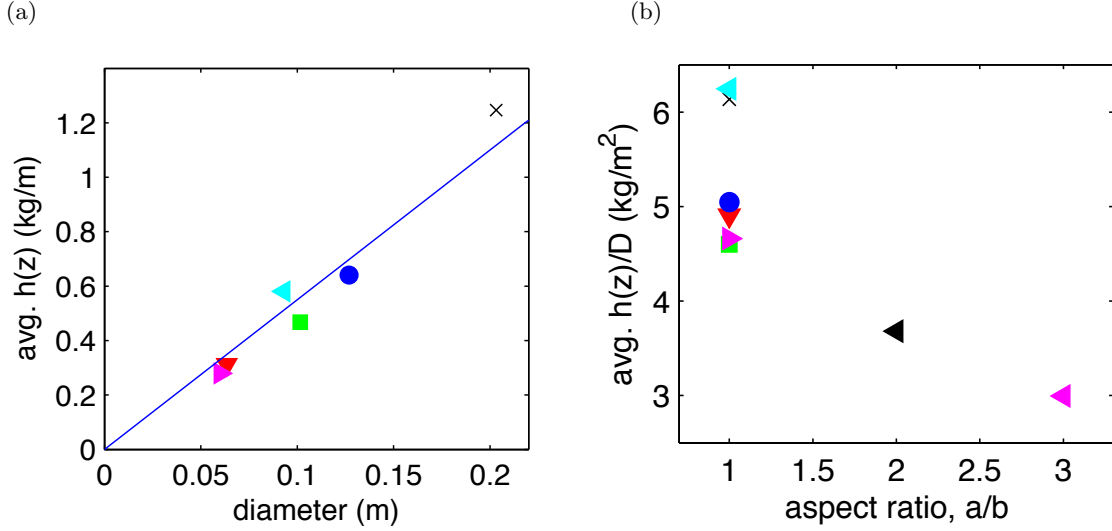


FIG. 3: (a) Plot of the average  $h(z)$  for circular-nosed intruders versus  $D$ , which shows that  $h(z) \sim 5.5D$ . (b) Plot of the average  $h(z)/D$  versus the intruder aspect ratio,  $a/b$ , which shows a substantial decrease  $h$  as the intruder nose is elongated.

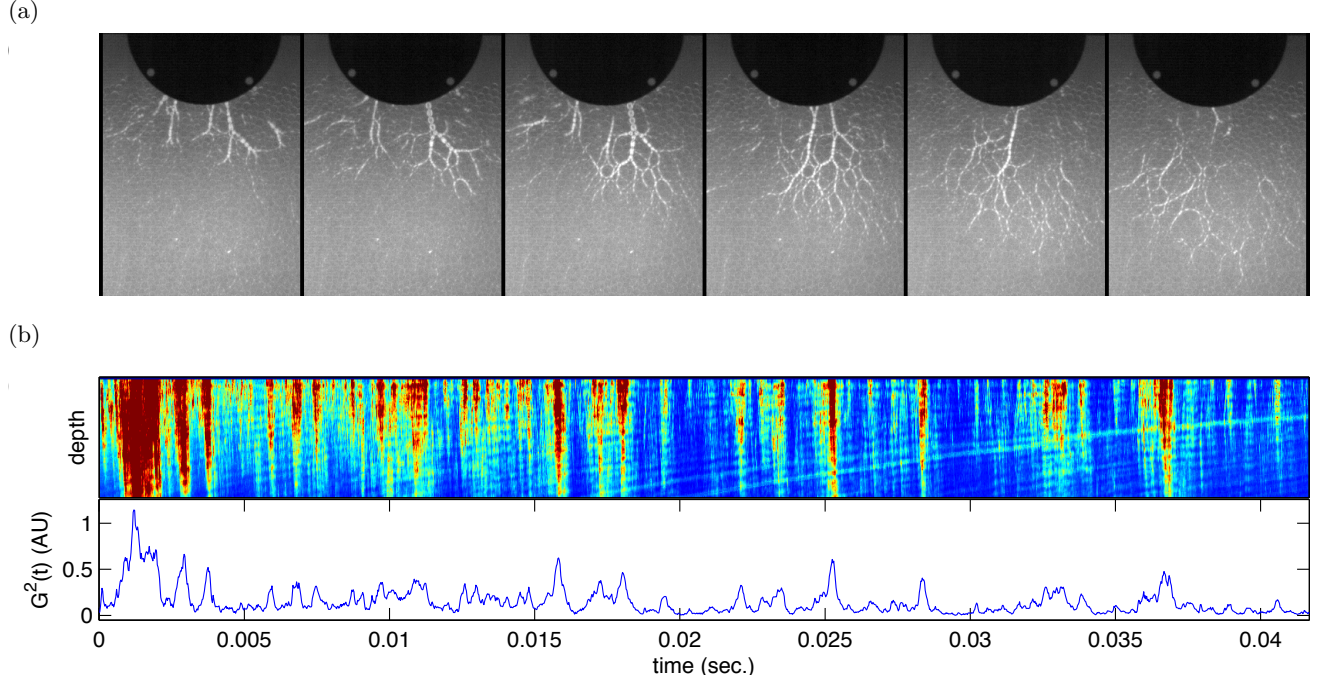


FIG. 4: (a) Six frames (starting at 2.75 ms after impact and spanning 475  $\mu$ s) showing how forces propagate from the intruder into the granular material. (b) A space-time plot for the response under the bottom half of the intruder over time (x-axis is time, and y-axis is radial distance from the intruder, spanning roughly 10 particle diameters). The slope of these lines gives a force propagation speed of roughly 300 m/s. (c) The sum of the response in the space-time plot above, with background lighting subtracted. This time series yields a measurement of instantaneous force on the intruder, where the range shown above (0 to 1.1 AU) maps to an acceleration range of 0 to 27 g.

transmitted to the intruder? We can provide at least a partial answer to that question by matching the photoelastic signal to the measured acceleration of the intruder. This acceleration is determined by tracking the center of mass of the intruder, and then differentiating twice. Numerical differentiation accentuates the tracking errors, and it is necessary to low-pass filter the computed intruder acceleration with a cutoff which we set to 133 Hz. The photoelastic response is obtained by summing the pixel values in the photoelastic images in a region beneath the intruder (after correcting for inhomogeneity in the background lighting). We then filter the photoelastic response in a manner similar

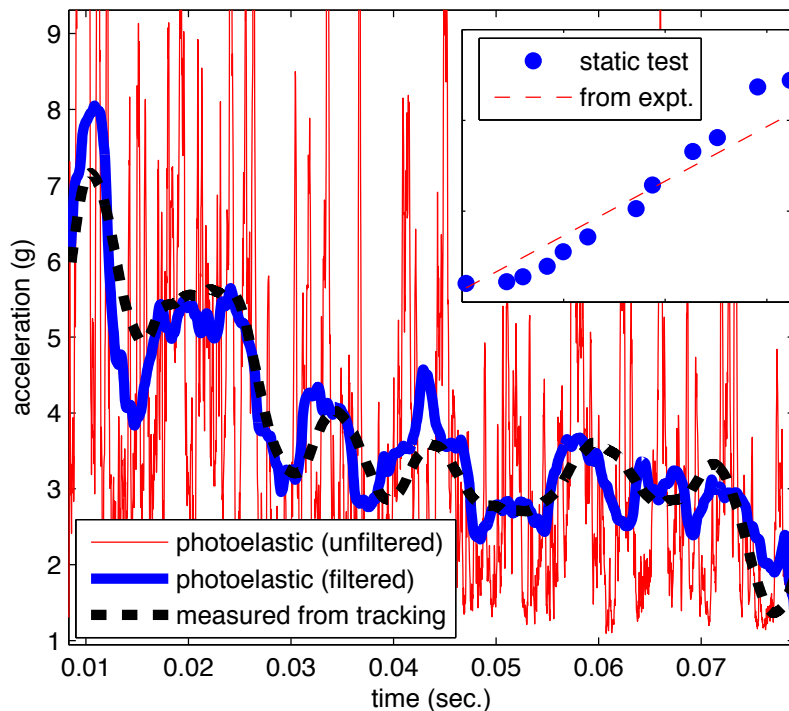


FIG. 5: Plot showing good correlation between acceleration fluctuations and photoelastic response. The acceleration measurement (black, dashed line) requires time-filtering which limits the high frequency resolution. We average the photoelastic response from Fig. 4(b) such that the frequency resolution is the same as for the acceleration (blue line). With a linear rescaling of the photoelastic measurement, we observe extremely close agreement, both for the mean and fluctuations. The thin red line shows the calibrated photoelastic force measurement without time-filtering, which shows very large fluctuations at short time scales.

to the acceleration, and find that there is a very good agreement between the filtered photoelastic force signal and the intruder acceleration, as in Fig. 5. This suggests that the photoelastic fluctuations (red curve in Fig. 5) correspond to fast, physical, force fluctuations acting on the intruder.

The scenario that we suggest is that as the intruder plows through the granular material, it collides with a latent network, which then responds by carrying momentum and energy into the material. By latent, we mean that a subset of grains are initially positioned so that when the intruder strikes, they can respond as a ‘stiff’ network, even though they were not necessarily strongly compressed before impact. A slightly different scenario is to think of the parts of the network as relatively independent ‘clusters’ that collide with the intruder. A cluster here is highly anisotropic—i.e. it is a quasi-linear collection of particles.

We further pursue the nature of the force fluctuations and their connection to a collisional damping term by normalizing the force signal by the ‘slow time’ drag force,  $F_{slow}$  (i.e., a low-order polynomial fit to  $F(t)$ ) signal, to produce data such as Fig. 6(a). In Fig. 6(b) we show the time correlation function of the fluctuating term,  $\eta = F(t)/F_{slow}$ , which decays with a characteristic time of  $\tau_d \simeq 1$  ms. We also determine the penetration range of the strong force network vs. depth below the intruder, as in Fig. 7. These data are consistent with an exponential decay of the strong response vs. distance below the intruder, with a decay length of  $L_d \simeq 10d$ , where  $d$  is a mean grain diameter of roughly 5 mm. Note that the ratio of decay length to the decay time is  $L_d/\tau_d \simeq 50$  m/s, which is faster than the intruder speed (roughly 5 m/s) and slower than the granular sound speed (roughly 300 m/s) for the material shown here.

## COLLISIONAL MODEL

Our observations thus far suggest that momentum is transferred to the granular material through intermittent collisions with a force network, sending momentum and energy away in the form of pulses. To capture the basic physics of this process, we will present a model that assumes collisions with grain ‘clusters’, which are understood to

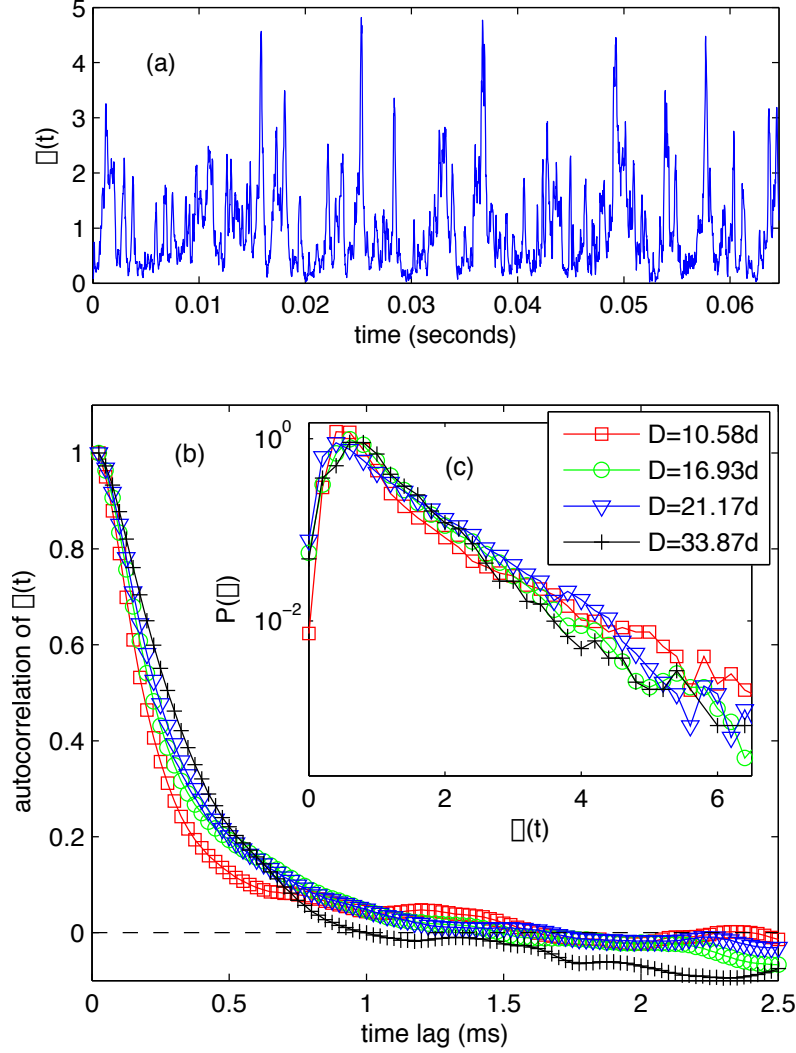


FIG. 6: (a) Plot of  $\eta(t)$  for a single experiment (typical of all experiments), where  $\eta(t) \sim F(t)/F_{slow}(t)$ , as discussed in the text. (b) The autocorrelation and (c) the PDF (semi-log scale) of the combined fluctuating signals for all experiments for each intruder ( $\sim 20$  experiments per intruder). We observe  $P(\eta) \sim \exp(-\eta)$  with an autocorrelation length of roughly 1 ms, which gives a typical event time, in agreement with Fig. 4.

be collections of particles forming part of the strong force network. These collisions occur along the lower boundary of the intruder at random locations (during the course of a complete impact). The model contains several assumptions:

- Momentum transfer from intruder to granular material takes place by discrete collisions with clusters (as discussed above) with a typical mass which is large compared to that of a grain, but small compared to the system size.
- Collisions occur, and transfer momentum in the direction normal to the intruder boundary. This assumption is generally consistent with visual inspection of the force chain directions.
- Collisions occur inelastically with a typical restitution coefficient,  $e$ .
- The rate of collisions is set by the instantaneous intruder speed,  $v$ .

These assumptions lead naturally to collisional damping proportional to  $v^2$ . Additionally, it is possible to test this picture by considering how the shape of the intruder affects the dynamics. If, as in Fig. 8,  $\hat{n}$  is the local normal to the lower boundary of the intruder, then the force acting on the intruder from a collision is

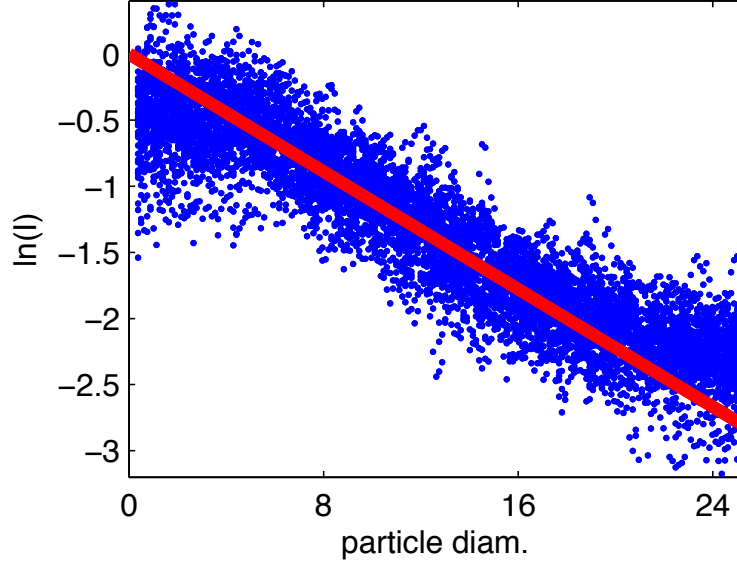


FIG. 7: Using a thin angular slice (width of  $\pi/8$  radians) centered directly beneath the intruder for the 10 fastest experiments for one intruder size, we identify the 4 largest acoustic pulses in each run. We then plot the natural logarithm of acoustic intensity versus depth for each pulse, normalized by the total intensity in the pulse. The red line shows a fit of  $\exp(-r/L)$ , where  $L$  is the decay length. For this intruder, we observe a decay length of about 10 particle diameters.

$$\vec{f} = \frac{\Delta \vec{p}}{\Delta t} = \frac{(1+e)v^2 \cos^2 \phi}{\gamma d} \left( \frac{m_c m}{m_c + m} \right) \hat{n}. \quad (6)$$

The  $z$ -component of the total force acting on the intruder is then

$$\begin{aligned} F_z &= \int d\vec{F} \cdot \hat{z} \\ &= \frac{(1+e)\beta m_c m}{\gamma d^2 (m_c + m)} \left[ \int_{-W/2}^{W/2} dx (1 + C'^2)^{-1} \right] v^2 \\ &= B_0 \cdot I[C(x)] \cdot v^2. \end{aligned} \quad (7)$$

The total torque,  $\vec{\tau}$ , about the center of mass of the intruder is given by integrating  $\vec{r} \times \vec{f}$  over all collisions at the intruder surface, similarly to Eq. 7:

$$\begin{aligned} \vec{\tau} &= \int \vec{r} \times \vec{f} \frac{\beta}{d} dl \\ &= B_0 v^2 \int \vec{r} \times \hat{n} \cos^2 \phi dl \end{aligned} \quad (8)$$

Here,  $\vec{r} = x\hat{x} + C(x, \theta)\hat{z}$ ,  $\hat{n} = -\sin \phi \hat{x} - \cos \phi \hat{z}$ , and  $\sin \phi = -C'(1 + C'^2)^{-1/2}$ , with  $dl = (1 + C'^2)^{1/2} dx$  and  $\cos \phi = (1 + C'^2)^{-1/2}$ , as before (see the sketch in Fig. 8). This yields:

$$\begin{aligned} \vec{\tau} &= B_0 v^2 \int dx \left( \frac{CC'}{1 + C'^2} + \frac{x}{1 + C'^2} \right) \hat{y} \\ &= B_0 J[C(x, \theta)] v^2 \hat{y}. \end{aligned} \quad (9)$$

The mean force and torque expressions contain boundary integrals which explicitly depend on boundary shape. The constant  $B_0 = (1+e)\beta m_c m / (\gamma d^2 (m_c + m))$  contains various system parameters that we assume to be nominally

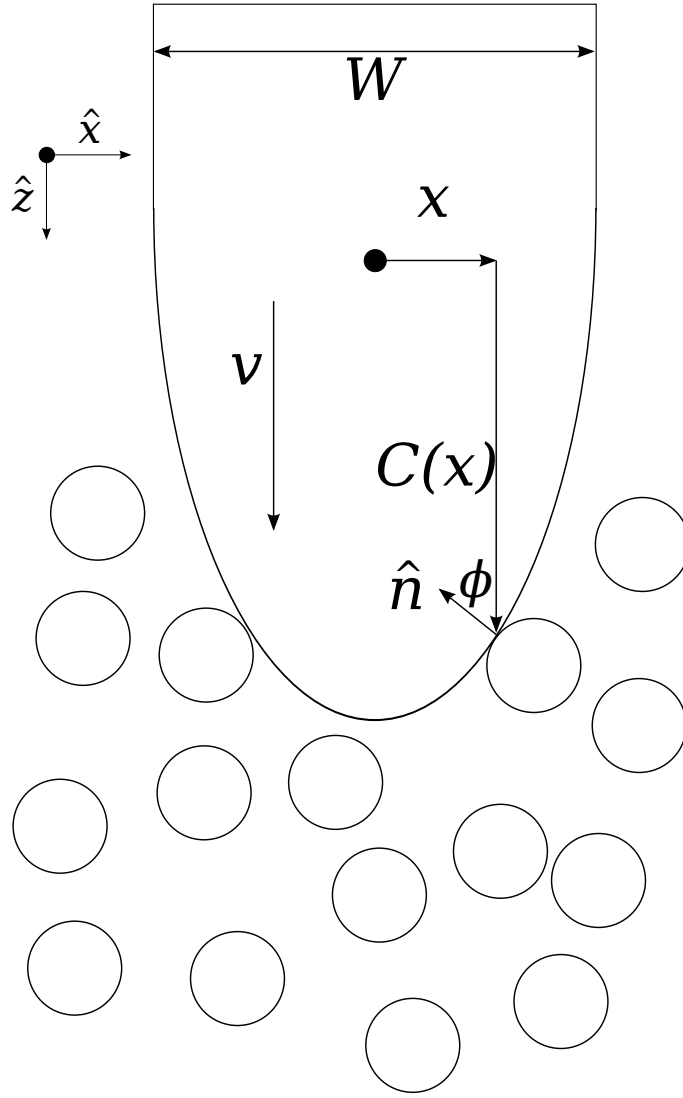


FIG. 8: Sketch of the collisional model, where an intruder of width  $W$  randomly collides with grain clusters (represented by the open circles) as it moves at velocity  $v$ . The collisions occur along the ‘nose’, i.e. the leading edge of the intruder, at positions  $\vec{r} = x\hat{x} + C(x)\hat{z}$  measured from the center of mass. These collisions involve momentum transfer normally into the intruder, along normal vector  $\hat{n}$ .

the same for all intruders striking a particular material. The size and shape effects are contained in  $I[C(x)]$ , defined as:

$$I[C(x)] \equiv \int_{-W/2}^{W/2} dx (1 + C'^2)^{-1}, \quad (10)$$

and in the corresponding functional  $J$  for the torque. By construction, the force on the intruder is proportional to  $v^2$ . There is, in principle, only one free coefficient,  $B_0$ , which contains all the unknown material-dependent properties, such as the effective coefficient of restitution and the mass of a cluster. However, we find that if the intruder has a sharp tip, then this single-coefficient approach must be replaced by two terms: one for the tip, and one for the rest of the intruder surface.

To test this model, we determine the coefficient  $h(z)$  for intruders of different shapes: circular, ogive, and triangular. By ogive, we mean any shape consisting of a horizontally symmetric convex curved leading edge of the intruder, such as half of an ellipse, joined above to a straight rectangular tail, as in the sketch of Fig. 8.

Triangular intruders are particularly simple because the shape integrals involve a constant slope,  $s$  for the leading edge. In Fig. 9 we show typical photoelastic images from high speed videos of triangular intruder impacts. Here,  $s$



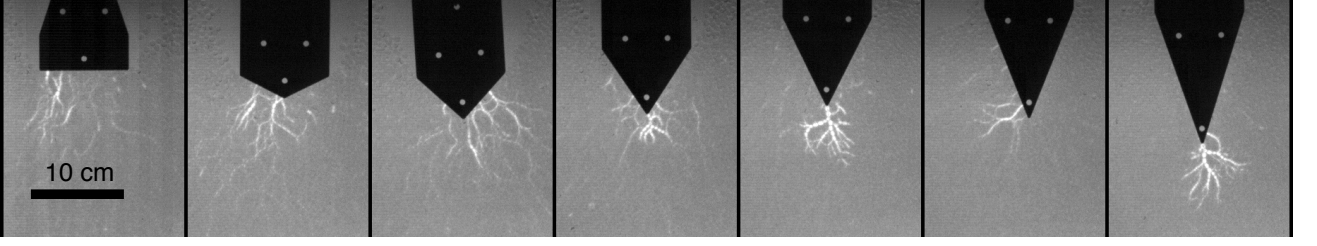


FIG. 9: Still frames showing the seven triangular-nosed intruders with slope  $s = 0$  to  $s = 3$  (increments of 0.5), from left to right. These images are chosen during photoelastic events. Note that the force chains are roughly normal to the intruder-granular interface. Additionally, these images illustrate that, when  $s$  is large, significant forces occur at the intruder tip.

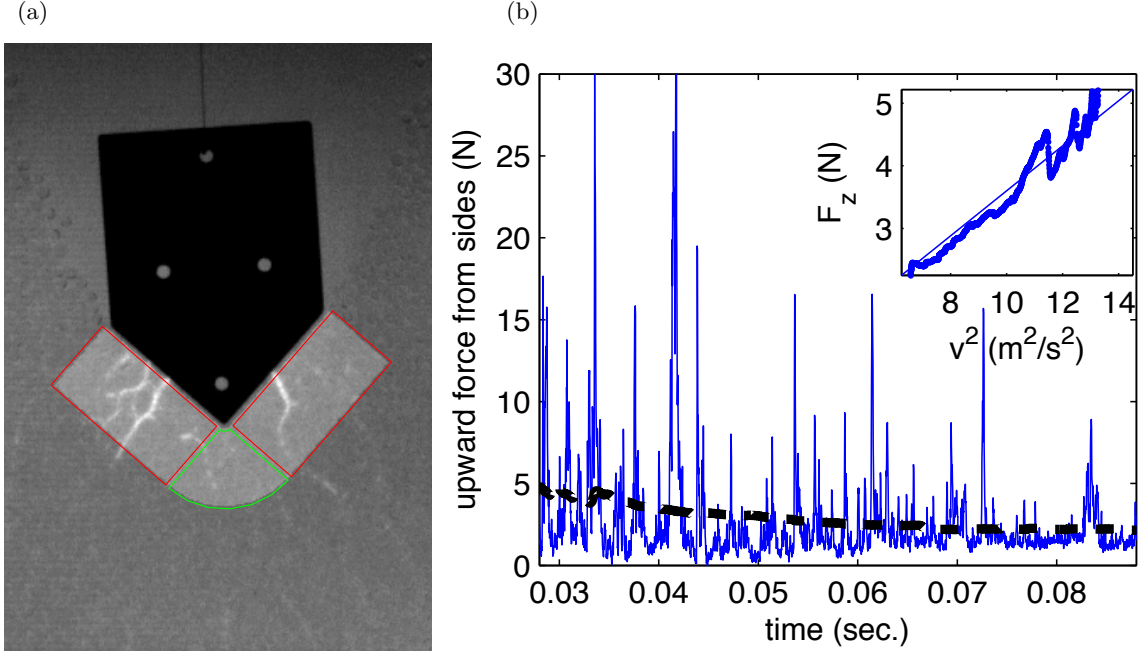


FIG. 10: (a) A photoelastic image showing the different regions used to measure the force contributions from the sides (outlined in red) and from the tip (outlined in green). (b) Plot of calibrated photoelastic force on the sides of the  $s = 1$  intruder, for a single trajectory with  $v_0 \approx 3.8$  m/s, both at each frame (thin, blue line) and after a low-pass filter (thick, black, dashed line). Inset shows the low-pass filtered force signal determined photoelastically vs.  $v^2$ , with a fit line through the origin with slope 0.36, which is the effective drag coefficient contribution from the sides of the triangular intruder in this case.

is the magnitude of the slope of the lower parts of the intruder relative to the horizontal direction. For the more pointed triangles, it is clear that the tip is more effective than the rest triangle boundary at generating a strong force response. When analyzing triangles, we consider the photoelastic response from the tip region separately from the response on the edges, as in Fig. 10, top.

Since  $h(z)$  is nearly constant, after small initial transients, we show results in Fig. 11 for  $h_0$ , the constant part of  $h$ , vs. the triangle slope,  $s$ . In this figure, we separate the contributions from the tip and the flat surfaces. Note that for the former, this effect is zero for  $s = 0$ , and then asymptotes to a constant value as  $s$  grows.

In Fig. 11(b), we show data for all shapes, plotted as  $h_0$  vs. the shape factor from the collision model,  $I[C(x)]$ . The data are in good agreement with the prediction from the model. The proportionality constant,  $B_0 \simeq 7.62$ , then encompasses all the unknown particle properties.

The model also provides information on the torque which is exerted on the intruder. If a non-circular intruder is dropped with a perfect vertical orientation, then the net torque is zero (discounting the possibility that instantaneously, the torque may not be zero, due to fluctuations associated with collisions.) However, if the inclination of the vertical axis of an intruder is not vertical, then there is a net torque, which may be stabilizing, i.e. turning the intruder

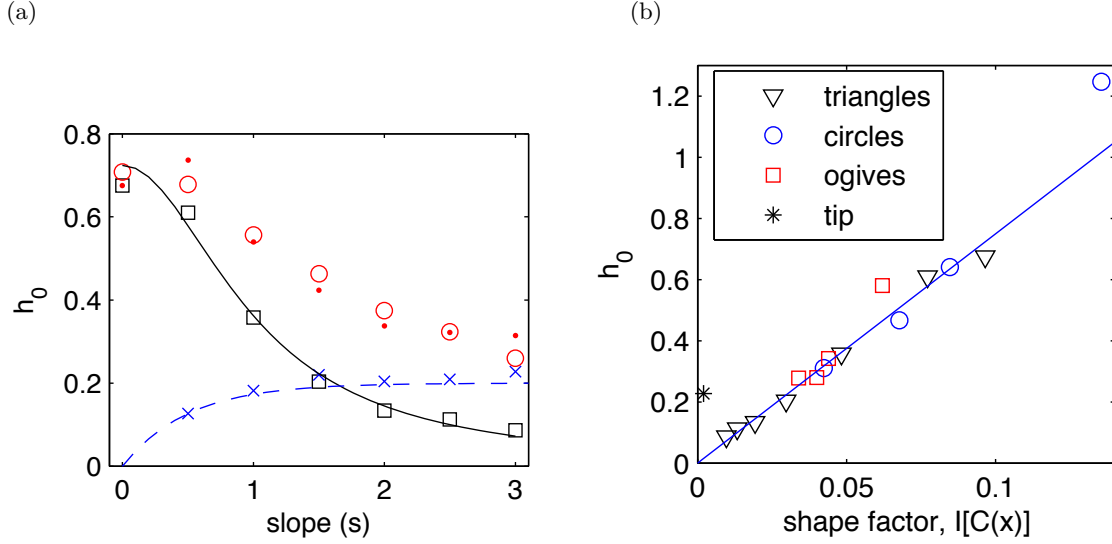


FIG. 11: (a) Plot of  $h_0$  measured from the intruder acceleration and force measurements inferred from the photoelastic response. The measurements from intruder acceleration (open, red circles) and from the photoelastic signal (red dots) show good agreement. The contribution from the tip (blue crosses), measured from the photoelastic signal, stays relatively constant for  $s > 1$  (fit line is  $0.2(1 - e^{-2s})$ , an approximate fit assigned by eye). Open, black squares show the contribution from the sides, which matches well to the model (solid black line),  $I(s) = W(1 + s^2)^{-1}$ , as in Eq. (??). (b) Plot of  $h_0$  versus  $I[C(x)]$  for all intruders. The solid line shows a linear fit through the origin with slope  $\frac{h_0}{I[C(x)]} = B_0 \approx 7.6$ . The  $h_0$  value for triangular noses is the photoelastic measurement from the sides (excluding the tip), while the asymptotic value (approximately 0.2 N) for the tip measurement is shown separately (black asterisk). See Refs. [9, 10] for further discussion.

back towards vertical, or destabilizing, i.e. tilting the intruder further from vertical. The details of the intruder boundary shape and the position of its center of mass both play a role in determining stability. The net torque on the intruder yields a second-order-in-time differential equation for the angle,  $\theta$  which measures the inclination from vertical. With some approximations [10], this equation can be converted to a second order differential equation for  $\theta(z)$ . Stability of the intruder to rotation is then determined by the eigenvalues of the characteristic roots of this equation. Any positive eigenvalue implies instability, and in such a case, the most positive eigenvalue,  $\lambda_+$ , dominates the evolution of  $\theta$ :  $\theta(z) \propto e^{\lambda_+ z}$ . In Fig. 12, we show data for unstable cases, which indicate an exponential growth of  $\theta$ . From our collision model, we calculate the corresponding growth rate, where now there are no longer any adjustable parameters. As shown in Fig. 13, the measured and predicted growth rates are in reasonable agreement. For details of the calculations, see [10].

## IMPACTS AT HIGHER SPEED

Until this point, we have focused on the regime where the intruder speed is much smaller than the speed of force transmission in the granular material. In fact, we have taken this fact for granted in the collisional model presented in the previous section, since we assume the collisions are randomized and point-like over the leading edge of the intruder. However, we have not considered what sets the velocity scale for these grain-grain collisional processes which lead to the primary drag on the intruder for the previous experiments. One might expect that if the intruder speed became similar to the grain-grain force transmission speed, the results presented in the previous sections may no longer be valid. As the intruder's and granular force transmission speeds become comparable, how does the nature of the force response change, both at the grain scale and macroscopically? For more information on the material presented in this section, see [26].

We distinguish three relevant speeds during impact: the speed of the intruder,  $v$ , the speed of sound in the material from which the grains are made,  $v_b$ , and the speed of the propagating signal along the strong force network,  $v_f$ . The speed of information propagation along the force network is set by the force law for interactions between grains. In general, this law does not depend linearly on the compression of the interacting grains. Rather, if the distance between

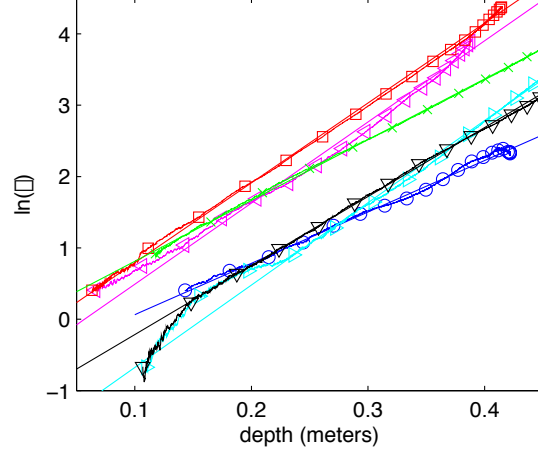


FIG. 12: Plot of the natural log of the angular deviation versus depth from single trajectories, where all angular deviations are considered positive. The straight lines suggest exponential growth for  $\theta$  vs. depth; the slope on the semi-log plot corresponds to the exponential growth rate,  $\lambda_+$ , as discussed in the text.

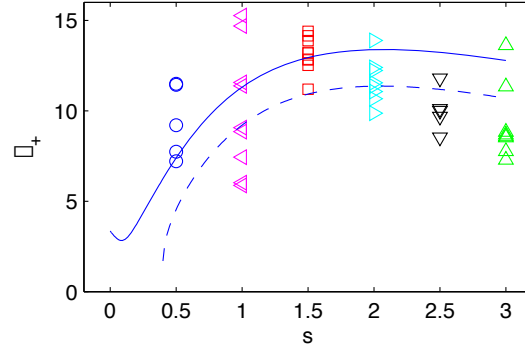


FIG. 13: A plot of all measured values of  $\lambda_+$  versus the aspect ratio,  $s$ . Each data point represents a trajectory with sufficient angular deviation (i.e., it has at least 3000 data points where  $\theta > 10^\circ$ ), where we measure the growth rate as shown by the linear fits imposed on each trajectory in Figure 12. Also plotted is the prediction for  $\lambda_+$  from the collisional model with (solid line) and without (dashed line) the contribution from the intruder tip (see Ref. [10] for details).

the centers of two grains,  $x = R_i + R_j - \delta$ , is smaller by  $\delta$  than the sum of their radii, the force typically has the form

$$f = k\delta^\alpha \quad (11)$$

where  $\alpha = 3/2$  is the Hertz exponent if the particles are elastic spheres. By direct measurement, we typically find for our photoelastic disks  $\alpha \simeq 1.4$ . The constant  $k$  depends on the elastic properties from which the materials are made. These same elastic properties determine the bulk material sound speed,  $v_b$ . We note, that although purely two-dimensional calculation with linear elasticity predicts  $\alpha = 1$  for disks, we always measure  $\alpha \simeq 1.4$  for typical disks used in these experiments. This finding may be due to the fact that the disks can expand in the third dimension, to imperfections in disk surface, or possibly to other effects.

As force is carried down a force chain, the time scale for transmission from one grain to the next is the collision time,  $t_c$ , which is set by the force law:

$$t_c = dv_0^{\frac{1-\alpha}{1+\alpha}} v_b^{\frac{-2}{\alpha+1}} C(\alpha), \quad (12)$$

where  $C(\alpha)$  depends on  $\alpha$  but otherwise is a constant. Note that  $t_c$  is much longer than the time  $d/v_b$  for stresses to propagate a distance  $d$  at  $v_b$ , where  $v_b = (E^*/\rho)^{1/2}$  is the bulk sound speed, and  $d$  is the mean grain diameter. Here,  $E^*$  is an effective elastic modulus, and  $\rho$  is the mass density of the grains (which we determine experimentally); see Experimental Techniques section below for more information.

The speed of force propagation down a chain is set by  $t_c$  and the diameter,  $d$  of a grain:

$$v_f \propto d/t_c \quad (13)$$

or,

$$v_f \propto \frac{d}{t_c} = v_0^{\frac{\alpha-1}{\alpha+1}} v_b^{\frac{2}{\alpha+1}} [C(\alpha)]^{-1}, \quad (14)$$

If energy is conserved, then  $t_c$  is given by eq. 12. However, a similar scaling still applies even if energy is not conserved, as long as the energy loss is not too great.

This leads to a scaling relation involving ratios of  $v_f$ ,  $v_0$ , and  $v_b$ :

$$\frac{v_f}{v_b} \propto \left( \frac{v_0}{v_b} \right)^{\frac{\alpha-1}{\alpha+1}}. \quad (15)$$

which forms the basis for understanding the speed of front propagation as a function of impact speed and material properties. Note that Gomez et al.[27] have obtained a similar relation for systems of frictionless grains, where they have invoked equipartition between potential and kinetic energy of grains. The present argument, is based on the fact that in systems of frictional grains, for which there is no well defined conserved energy, the force is carried along sometimes-tenuous strong force networks, which are strongly loaded and then unloaded by impact.

To significantly vary the ratio of relative speed of impact,  $v_0$ , to the speed of propagation along the strong network,  $v_f$ , i.e.  $M' = v_0 t_c / d \sim v_0 / v_f$ , we use materials of three different stiffnesses. By these means, we can vary  $M'$  by over two orders of magnitude. In Fig. 14, we contrast frames from impacts at low, moderate and high  $M'$ . In evaluating  $M'$ , we use the assumption, justified below, that  $v_f \propto d/t_c$ . A key observation is that for the lowest  $M'$ , the force is carried primarily over a filamentary force network (bright particles in the upper image of Fig. 14.) As  $M'$  increases, the strong force network becomes increasingly dense, so that for the largest  $M'$  case, the propagating force network is spatially dense and not filamentary.

We coarse-grain frames from impact events to obtain a coarse-grained space-time plot of the photoelastic response as a function of time and depth under impacting intruders. Fig. 15 shows the space-time plots corresponding to the impacts shown in Fig. 14. This smoothing averages over force networks, although these are an essential feature of the signal propagation. We then plot the measured front speeds vs. the initial impact speed,  $v_0$ , in the lower left part of Fig. 15. The data fall on separate curves for each type of particle material, and a fit to these data is in good agreement with Eq. 14. All of these data can be collapsed onto a single curve, as suggested by Eq. 15.

There is a departure from the power-law scaling of Eq. 14 and Eq. 15 at the highest  $M'$ , which also corresponds mostly to impacts into the softest material. We show an alternative characterization of this effect in Fig. 16, top, in the form of a plot of  $v_f/(d/t_c)$  vs.  $M'$ . Note that at high  $M'$  the forces are no longer carried on a filamentary network, and for the strong forces involved in this case, extra contacts can form, strengthening the material. We further characterize this effect also through a participation ratio,  $P$ , defined as the fraction of particles carrying large forces.  $P$  rises steadily with  $M'$ , and begins to approach an asymptotic value of order unity at roughly a similar value of  $M'$  where the ratio  $v_f/(d/t_c)$  begins to rise. We note two phenomena connected to the departure at high  $M'$  from the power-law scaling in Eqs. 14 and 15. One is that the number of particles in the strong network grows with  $M'$ , since the force transmission slows relative to the rate at which new parts of the network are created. The other phenomenon is that under strong enough forcing, new contacts form, which strengthens and homogenizes the force structure.

## SIMULATION RESULTS FOR PENETRATION DEPTH AT LARGE $M'$

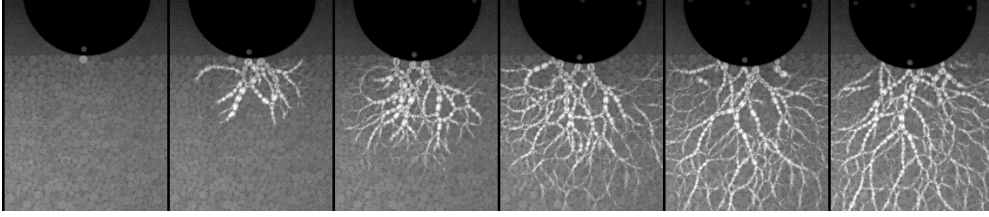
Numerical simulations provide a useful tool in the study of granular materials, in particular since, in a simulation, vs. an experiment, it is much easier than in an experiment to change the system parameters, such as friction, particle size, particle stiffness. The discussion given here is focused on the influence of system parameters on the penetration trajectory. More in-depth analysis can be found in [28], and the details about the simulations are given in the Techniques section. We note that simulations using a nonlinear force model ( $\alpha \neq 1$ ) are in progress and will allow more detailed comparison to experiments.

We start by considering a randomly packed system with particles characterized by polydispersity  $r = 0.2$ , so that the particle sizes are uniformly distributed in the range  $d(1 \pm r)$ , where  $d$  is the average particle diameter,  $\mu = 0.5$

(a)



(b)



(c)

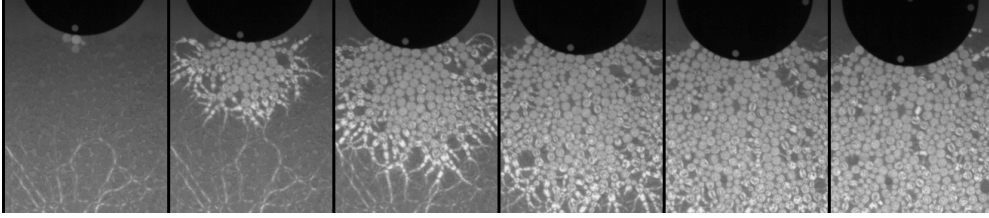


FIG. 14: Frames showing force propagation after three impacts with  $v_0 \approx 5$  m/s. (a) The hardest particles ( $M' \approx 0.1$ ) correspond to fast, chain-like force propagation. (b) Forces for intermediate stiffness particles ( $M' \approx 0.3$ ) are more dense spatially, but still relatively chain-like. (c) The softest particles ( $M' \approx 0.6$ ) show a dense force structure which propagates with a well defined front.

is the static friction coefficient,  $e = 0.5$  is the coefficient of restitution. The simulations discussed here only have kinetic friction (viscous damping) only, so that tangential springs at the point of contact are removed ( $k_t = 0.0$ ), as discussed in the Techniques section. The normal forces are modeled by linear springs, so that  $\alpha = 1$  here. The intruder is a disk, with diameter  $D_i = 10$  in units of  $d$ , and otherwise possessing the same material properties as the granular particles. Figure 17 shows the time evolution of  $z(t)$  of an intruder impacting the granular bed with one of seven different speeds, ranging from 0.05 to 1, scaled by  $d/\tau_c$ , where  $\tau_c$  is a typical binary collision time between the particles (impact speed independent for the linear force model considered here).

The key results presented in Fig. 17 are as follows. As expected, slower initial impact speeds,  $v_0$ , create shallow craters; specifically, the penetration depth is less than the intruder's own diameter. By contrast, intruders of higher speeds are entirely submerged in the granular bed. For the larger impact velocities, we find an overshoot in the penetration depth, i.e., the intruder rebounds towards the surface of the granular layer, as also observed experimentally [5, 29]. Next, we proceed to analyze the influence of the properties of the granular system on the penetration depth.

Figure 18 shows the influence of elasticity of the granular particles, measured by the coefficient of restitution,  $e$ . A large coefficient of restitution leads to a significantly deeper penetration, as might be expected, since the energy loss is reduced relative to a lower restitution coefficient. Interestingly, while a decrease of  $e$  reduces the depth of penetration, it does not remove the overshoot of the  $z(t)$  curve. We will see below that a different behavior results when the frictional properties of granular particles are modified.

The influence of friction between the granular particles on the trajectory,  $z(t)$ , in particular, and on the response of the granular material to an intruder in general is not immediately obvious. For example, in considering the response of a system to a point force, it has been found that friction plays a role in determining how forces and stresses propagate

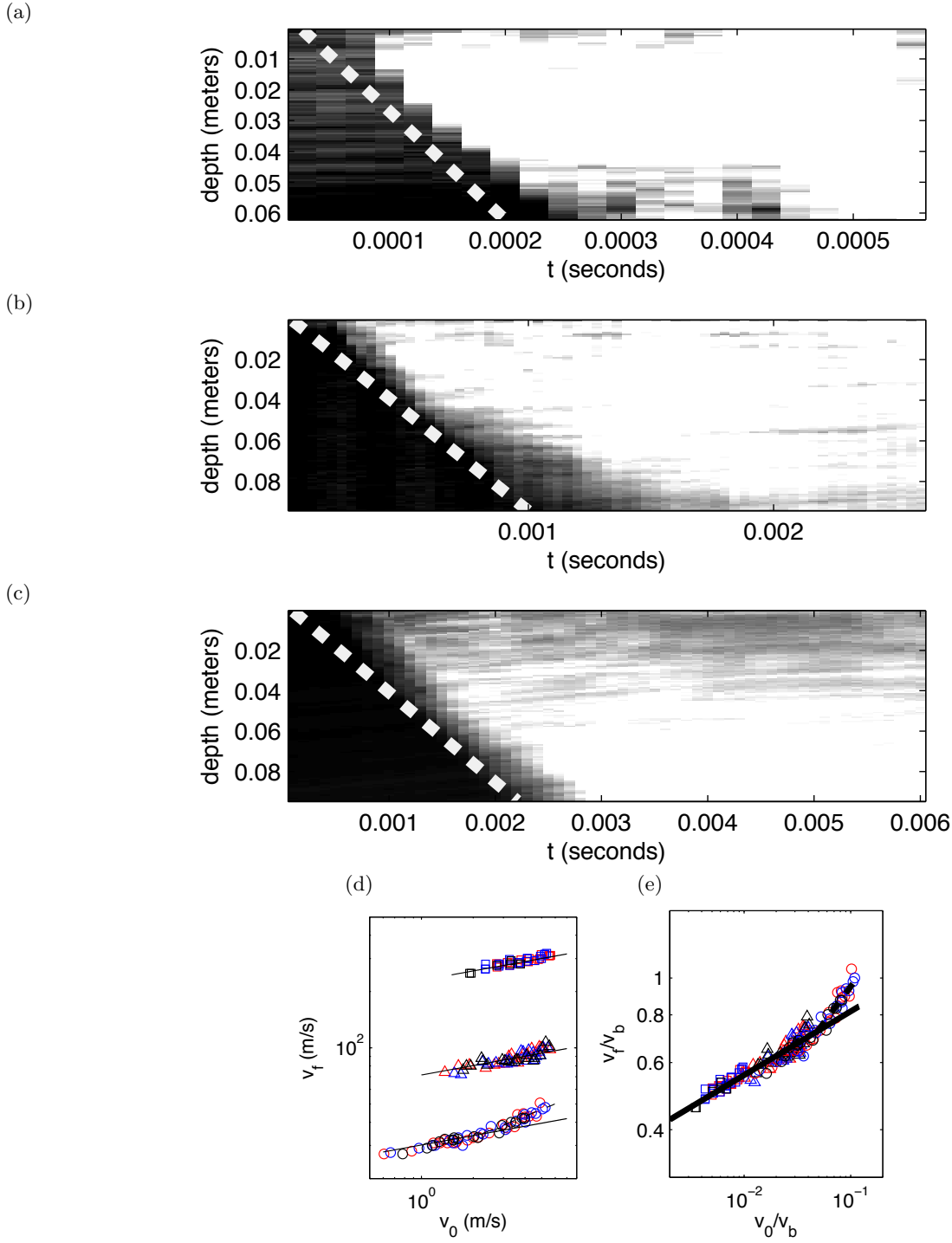


FIG. 15: (a)-(c) Space-time plots show forces propagating for impacts shown in Fig. 4 (see text for details). Dashed lines indicate  $v_f$ . (d) These are plotted versus  $v_0$ , where symbol shapes represent different particle stiffness (squares/triangles/circles represent hard/medium/soft particles), and symbol colors represent different intruder diameters (red/blue/black for 6.35/12.7/20.32 cm). (e) When velocities are normalized by the bulk sound speed these data collapse onto a single curve. The solid fit line corresponds to Eq. (15). The dashed fit line corresponds to collective stiffening of the soft particles for large deformations, as discussed in the text.

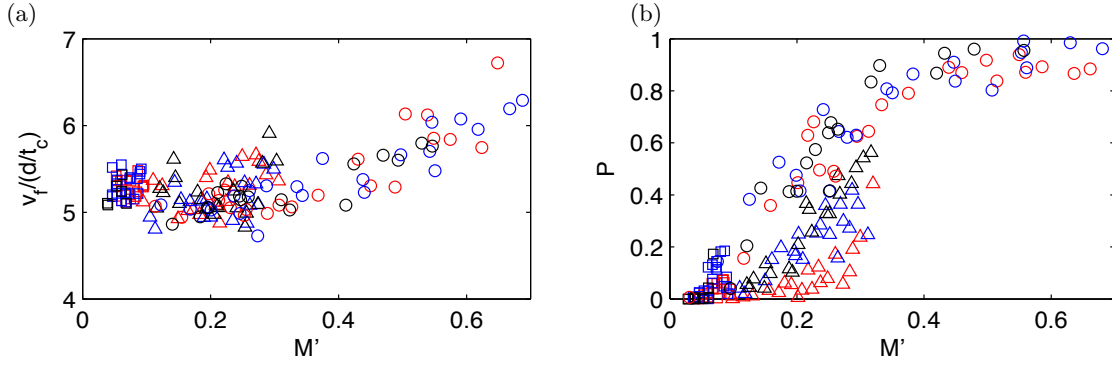


FIG. 16: (a) Ratio of measured propagation speed,  $v_f$ , to  $d/t_c$ , as a function of  $M'$ . The propagation speed for  $M' < 0.4$  is  $v_f \approx 5.3d/t_c$ . For  $M' > 0.4$ , the force propagation speed is faster than this relation. (b) Participation ratio,  $P$ , plotted as described in the text, as a function of  $M'$ . The spatial density of the forces saturates ( $P \approx 1$ ) when  $v_f$  departs from  $v_f \propto d/t_c$  for  $\alpha = 1.4$ .

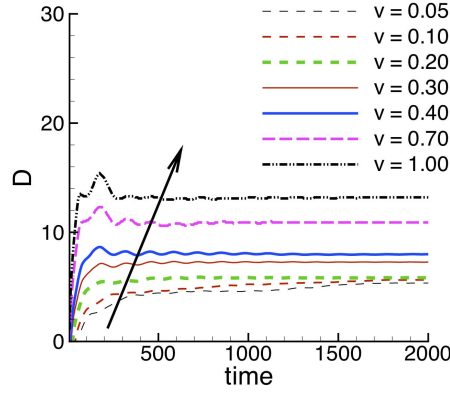


FIG. 17: Penetration depth of  $D_i = 10$  intruder impacting with different speed. Here we use  $r = 0.2$ ,  $k_n = 4 \cdot 10^3$ ,  $k_t = 0.0$ ,  $e = 0.5$ ,  $\mu = 0.5$ . Material properties of the intruder are the same as of the granular particles. The arrow shows the direction of increasing impact speed.

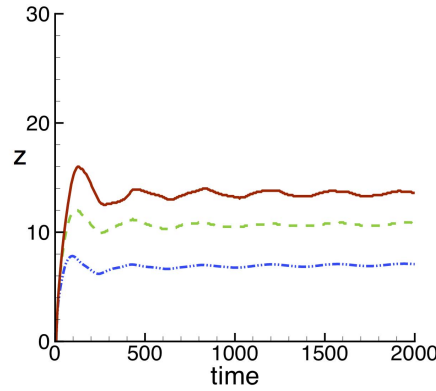


FIG. 18: Penetration depth of an intruder in systems with varying coefficient of restitution,  $e = 0.9$ ,  $0.5$ ,  $0.1$  shown by red (solid), dashed (green) and blue (dash-dot) lines, respectively. Here,  $v = 0.7$ , the system size is  $W = 200$ ,  $L = 200$ ; the other parameters are as in Fig. 17.

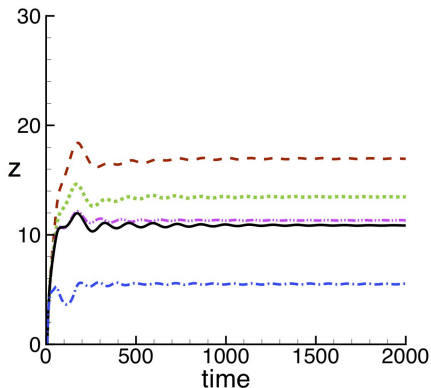


FIG. 19: Penetration depth for different friction models and Coulomb thresholds; here we show the results as follows (top to bottom):  $\mu = 0$  (red dashed);  $\mu = 0.1$ ,  $k_t = 0.0$  (green dotted);  $\mu = 0.1$ ,  $k_t = 0.8$  (pink dash-dot-dot),  $\mu = 0.5$ ,  $k_t = 0.0$  (black solid);  $\mu = 0.5$ ,  $k_t = 0.8$  (blue dash-dot). Here  $v = 0.7$ , the other parameters are as in Fig. 17.

through the system [30]. Of course, a response to an intruder is expected to be more complicated since it leads to a large scale rearrangement of granular particles, which is not expected in a response to a localized (small) point force. Indeed, it has been suggested that friction is not necessarily crucial in understanding this response [17].

To illustrate the influence of friction, we consider two effects: first, the effect of the friction model, and second, of Coulomb threshold. Figure 19 shows the corresponding results. We find that having a model with static friction leads to a significantly smaller penetration depth (blue dash-dotted curve in Fig. 19) than a model without static friction, particularly for a large Coulomb threshold. For a smaller Coulomb threshold, the influence of static friction is weaker, and the response of the system in that case turns out to be similar to the one obtained using kinetic friction only (compare green dotted and pink dash-dot-dot curves in Fig. 19). Furthermore, an ‘overshoot’ in the intruder depth may be removed in the case of (strong) static friction. This is one significant difference between the influence of friction and inelasticity on the intruder’s dynamics: in the case of increased inelasticity (smaller coefficient of restitution), we still find an ‘overshoot’, as in Fig. 18.

To summarize this section, the simulations show that the material properties of granular particles (in particular elasticity and friction) play a significant role in determining dynamics of the intruder in the regime considered. Future work shall discuss the influence of these and other parameters in the regimes relevant to experiments discussed in this review.

## TECHNIQUES FOR EXPERIMENTS AND SIMULATIONS

### Experimental Techniques

#### *Experimental Apparatus*

The experimental apparatus[8–10] consists of two Plexiglas sheets ( $0.91 \text{ m} \times 1.22 \text{ m} \times 1.25 \text{ cm}$ ) separated by a thin gap (3.3 mm), and filled by photoelastic disks (thickness of approximately 3 mm). We construct the intruders from bronze sheet (bulk density of  $8.91 \text{ g/cm}^3$  and thickness of 0.23 cm). We drop the intruders from a height  $H \leq 2.2 \text{ m}$ , through a shaft connected to the top of the thin gap containing the particles. This produces impact speeds  $v_0 \simeq (2gH)^{1/2}$ . A Photron FASTCAM SA5 records results at frame rates of 10,000, 25,000, and 40,000 frames per second for the soft, intermediate, and hard particles, respectively. We measure the intruder velocity at impact by locating the intruder with a circular Hough transform at each frame and computing the velocity with a numerical derivative. We use the intensity of the photoelastic image at each frame to compute space-time plots to study the spatial structure of forces and measure  $v_f$ . We estimate an approximate uncertainty in the propagation velocity for each impact to be  $\pm 5\%$ .

We use particles made from three photoelastic materials, each with a different stiffness. The softest material is polyurethane sheet (Precision Urethane) with a hardness rating of Shore 60A, cut into disks of 6 mm and 9 mm diameter. The second material is a stiffer polyurethane sheet (Precision Urethane) with hardness rating Shore 80A,



cut into disks with diameters of 6 mm and 9 mm. The stiffest material is PSM-1, (Vishay Precision Group) cut into disks with diameters of 4.3 mm and 6 mm. We measure the force versus compression for single particles in separate experiments. We find that, for compression between two plates (similar to particle compression in force chains), a single scaling relation captures the behavior of all types of particles

$$f = E^* w d \left( \frac{\delta}{d} \right)^\alpha, \quad (16)$$

where  $f$  is the compression force,  $w$  is the particle thickness,  $d$  is the particle diameter,  $\delta$  is the displacement, and  $\alpha \approx 1.4$  for all particles. The magnitude of the force law is the effective Young's modulus,  $E^*$ , which is set by properties of the bulk material, including effects from the Poisson ratio. We measure  $E^* \approx 3$  MPa for the Shore 60A material,  $E^* \approx 23$  MPa for the Shore 80A material, and  $E^* \approx 360$  MPa for the PSM-1 material.

### Photoelastic Techniques

The experiments described here use photoelastic particles. as used by a number of researchers[21, 23–25, 31–46]. The important feature associated with particles made from a photoelastic material is that they yield particle-scale force information.

If a disk or other quasi-2D object is illuminated by an incident beam of intensity  $I_0$  and placed between crossed circular polarizers, then the fraction of light intensity that emerges for a ray that has traversed this disk is given by an expression that connects the local shear stress,  $\tau = \sigma_2 - \sigma_1$ :

$$I/I_0 = \sin[(\sigma_2 - \sigma_1)CT/\lambda]. \quad (17)$$

The  $\sigma_i$  are the principal stresses in the object, evaluated at the location of the light ray;  $C$  is the material-dependent stress optic coefficient;  $T$  is the object thickness along the direction of transmitted light;  $\lambda$  is the wavelength of the light.

We use an empirical approach, similar to that described by Howell et al.[21]. The idea is that contact forces acting on a grain create stress fields inside the grain which cause the phase variable,  $(\sigma_2 - \sigma_1)CT/\lambda$ , inside the sine function of Eq. 17 to wrap through multiples of  $\pi$ . Where the phase variable is an integer multiple of  $\pi$ , the corresponding transmitted image region is a dark, and where the phase is an odd multiple of  $\pi/2$  it is bright. In a photoelastic image of such a grain, increasing applied contact forces increases the stresses (both pressure and shear stress) within the grain, and leads to an increasing density of light/dark fringes. Where these fringes appear in the image depends on the wavelength/color of the light. Since the pressure is a reflection of the mean normal forces on a particle, hence the internal stress, it is possible to calibrate a measure of the fringe density (or sometimes total intensity) against the pressure,  $P$ .

In these experiments, the forces due to impact cause the particles experiencing large forces to appear as bright in a photoelastic image, but in general we do not resolve fringes. For particles made from the harder materials, the brightness of a particle in an image suffices to yield the force acting on it. For the softest material, multiple fringes can appear in a particle. In this case, particles experiencing the largest forces may appear slightly dimmer than particles experiencing somewhat less force, since for the largest forces, the apparent particle brightness is averaged over light and dark fringes.

### Intruder Shape

The circular intruders are machined from bronze sheet (bulk density of 8.91 g/cm<sup>3</sup> and thickness of 0.23 cm) into disks of diameters  $D$  of 6.35 cm, 10.16 cm, 12.7 cm, and 20.32 cm.

We used four ogive intruders. The ogives consisted of a continuous piece of material, where the leading part was a half-ellipse truncated along the minor axis, with semi-major axis  $a$  and semi-minor axis  $b = D/2$ , terminated by a rectangular tail of length  $L$ . We used three different ellipses, with  $a/b = 1$  (half-circle),  $a/b = 2$ , and  $a/b = 3$ . We kept the width of the ogives constant,  $D = 9.3$  cm, and we varied  $L$  to keep the intruder mass constant ( $L = b = 4.15$  cm for  $a/b = 3$  case, longer for other ogives). By keeping the width and mass constant, we isolate shape effects. Additionally, we used one smaller ogive with  $a/b = 1$ ,  $b = 3$  cm, and  $L = 7.7$  cm.

The triangular-nosed intruders are comprised of a downward-pointing isosceles triangle, symmetric about the vertical axis, with opening angle  $2\alpha$ , attached to a rectangular tail of the same width as the base of the triangle,  $W = 9.65$  cm.

The noses of these intruders are clearly evident in Fig. 4. The length of the tail is varied to keep the total area,  $A = 0.0107 \text{ m}^2$ , and hence, mass,  $m = 0.219 \text{ kg}$ , constant for different opening angles of the nose (for reference, the  $s = 3$  intruder has a tail which is 3.81 cm long). Thus, the intruder nose has a constant magnitude slope  $s = \tan^{-1} \alpha$ , except at the tip, which is rounded with a radius of about 1.5 mm. Note that this is smaller than the particle radii, which are greater than and 4.3 mm. The  $s = 3$  intruder is turned upside-down and used as the  $s = 0$  intruder.

### Data Processing

At each frame, we use distinguishing features of the intruder to locate its center of mass relative to the initial point of impact and its angular position relative to the vertical direction with errors of less than 1 pixel (0.5 mm). This yields the intruder trajectory, and the rotation angle,  $\theta$ . By discrete differentiation, combined with a low-pass filter, we obtain the velocity and acceleration. Using the data for  $z(t)$ ,  $v(t)$ , and  $a(t)$  for many different trajectories with varying initial velocities, we fit to a force-law model such as Eq. (1). This allows us to experimentally measure  $f(z)$  and  $h(z)$  for each intruder. This process is described in detail in [9].

### Simulation Techniques

We consider a rectangular domain in two dimensions with gravity. The particles are polydisperse discs, with their diameters varying randomly in a range  $\pm r$  about the mean. The particle-particle and particle-wall interactions are modeled using the soft-sphere approach that includes friction and rotational degrees of freedom. We solve the following equations of motion for each particle:

$$\begin{aligned} m_i \frac{d^2 \mathbf{r}_i}{dt^2} &= \mathbf{F}_{i,j}^n + \mathbf{F}_{i,j}^t + m_i \mathbf{g}, \\ I_i \frac{d\boldsymbol{\omega}_i}{dt} &= -\frac{1}{2} d_i \mathbf{n} \times \mathbf{F}_{i,j}^t. \end{aligned} \quad (18)$$

The normal force is given by

$$\mathbf{F}_{i,j}^n = [k_n x - \gamma_n \bar{m} \mathbf{v}_{i,j}] \mathbf{n},$$

where  $r_{i,j} = |\mathbf{r}_{i,j}|$ ,  $\mathbf{r}_{i,j} = \mathbf{r}_i - \mathbf{r}_j$ , and the normal direction is defined by  $\mathbf{n} = \mathbf{r}_{i,j}/r_{i,j}$ . The compression is defined by  $x = d_{ave} - r_{i,j}$ , where  $d_{ave} = (d_i + d_j)/2$ ,  $d_i$  and  $d_j$  are the diameters of the particles  $i$  and  $j$ ;  $\mathbf{v}_{i,j}^n$  is the relative normal velocity.

The nondimensional force constant,  $k_n$ , is related to the dimensional one,  $k$ , by  $k = k_n m g / d$ , where  $m$  is the average particle mass,  $d$  is the average particle diameter, and  $g$  is Earth's gravity. All quantities are expressed using  $d$  as the length scale, the binary collision time

$$\tau_c = \pi \sqrt{\frac{d}{2gk_n}},$$

as the time scale, and  $m$  as the mass scale. Then,  $\bar{m}$  is the reduced mass, and  $\gamma_n$  is the damping coefficient related to the coefficient of restitution,  $e$ , by  $\gamma_n = -2 \ln e / \tau_c$  (e.g., Kondic [47]). We take  $e$  constant and ignore its possible velocity dependence [48]. For definitiveness, we typically use the physical parameters that are appropriate for **the softest** photoelastic disks [41], in particular  $d = 4 \text{ mm}$ ,  $k_n = 4 \cdot 10^3$ ,  $e = 0.5$ . The parameters entering the force model can be connected to the physical properties of the material (Young modulus, Poisson ratio) using the method described in Kondic[47].

The tangential force is specified by two different models, which can be conveniently described within the same framework. The basic approach is based on a Cundall-Strack type of model [49], where a tangential spring of zero length is introduced when a new contact between two particles forms at  $t = t_0$ . Due to relative motion of the particles, the spring length,  $\xi$ , evolves as

$$\xi = \int_{t_0}^t \mathbf{v}_{i,j}^t(t') dt',$$

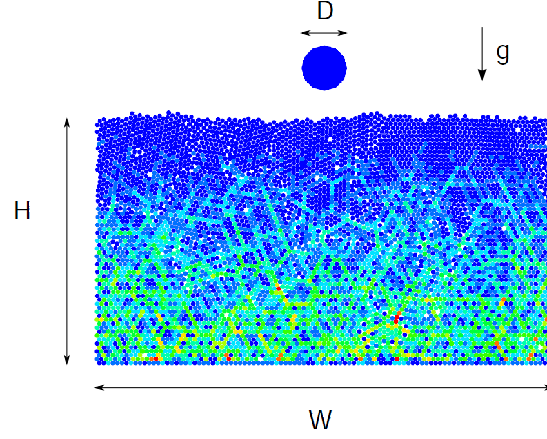


FIG. 20: System setup. Particles are colored according to the total normal force experienced (here only due to gravity).

where  $\mathbf{v}_{i,j}^t = \mathbf{v}_{i,j} - \mathbf{v}_{i,j}^n$ . For long lasting contacts,  $\boldsymbol{\xi}$  may not remain parallel to the current tangential direction defined by  $\mathbf{t} = \mathbf{v}_{i,j}^t / |\mathbf{v}_{i,j}^t|$  (see, e.g., [50, 51]); we therefore define a corrected  $\boldsymbol{\xi}' = \boldsymbol{\xi} - \mathbf{n}(\mathbf{n} \cdot \boldsymbol{\xi})$  and introduce the test force

$$\mathbf{F}^{t*} = -k_t \boldsymbol{\xi}' - \gamma_t \mathbf{v}_{i,j}^t,$$

where  $\gamma_t$  is the coefficient of viscous damping in the tangential direction (we use  $\gamma_t = \gamma_n/2$ ). To keep the magnitudes of tangential forces smaller than the Coulomb threshold, specified by  $\mu \mathbf{F}^t$ , where  $\mu$  is the coefficient of static friction, we define the tangential force by

$$\mathbf{F}^t = \min(\mu |\mathbf{F}^n|, |\mathbf{F}^{t*}|) \frac{\mathbf{F}^{t*}}{|\mathbf{F}^{t*}|}. \quad (19)$$

In addition,  $\boldsymbol{\xi}'$  is reduced to the length corresponding to the value of  $|\mathbf{F}^t|$  as needed. This is a commonly used model for static friction, with non-zero  $k_t$ . To be able to isolate the effect of static friction, we also consider a commonly used kinetic friction model based on viscous damping, which is obtained simply by putting  $k_t = 0$ . Therefore, depending on whether static friction effects are considered or not, we use either model 1:  $k_t = 0.8k_n$  (the value suggested in [52]), or model 2:  $k_t = 0.0$  (kinetic friction only). The exact value of  $k_t$  does not seem to be of relevance in the present context as long as  $k_t \neq 0$ . The particles making up the walls are made very inelastic and frictional, with  $\mu = 0.9$  and  $e = 0.1$ .

Figure 20 shows the system setup. Here,  $W$  and  $L$  are the width (depth) and the length of the granular bed, respectively. Periodic boundary conditions are implemented on the left and right boundaries. From below and above, the domain is bounded by rigid horizontal walls made up from monodisperse particles, with the properties as specified above. The role of the top wall is essentially to contain those few particles which would be ejected during particularly violent impacts. However, the upper boundary is positioned sufficiently high that collisions with this wall are very rare.

The simulations are typically carried out using 6000 particles, with the size of the domain, in units of the mean particle diameter, given by  $L = 100$  in the horizontal direction, and the initial height of the granular bed, given by  $W = 60$ , see Fig. 20. After settling, the particles form a system of height  $\sim 56d$  for random polydisperse systems.

The volume fraction,  $\rho$ , occupied by the grains is difficult to compute precisely due to the presence of a rough (on the grain scale) upper surface. Furthermore, some variations of  $\rho$  may also result due to different initial configurations. These variations are less than about 0.01, with typical  $\rho$ 's being in the range 0.85 – 0.86 for the random polydisperse systems. The influence of the change of simulation parameters, such as polydispersity, force constant, or gravity, leads to modifications of  $\rho$  on the same scale as different initial conditions. The influence of different initial conditions on large-scale features of the results, such as the final penetration depth, is minor, and therefore we expect that the influence of slight variations of  $\rho$  reported above is not significant.

## CONCLUSIONS

The preceding discussion is a summary of the grain-scale dynamics observed in a series of studies consisting of two-dimensional granular impact experiments and simulations. We have approached this problem from the perspective of a macroscopic force law which is dominated by a velocity-squared drag force. By using photoelastic disks and a high-speed camera, we have experimental access to the trajectory of the intruder as well as the force dynamics of the granular material at the smallest relevant space and time scales in the system. This yields microscopic data which has been previously inaccessible experimentally. **The simulations parallel the experimental results in the applicable parameter range.** The results from this work can be summarized as follows:

- 1) This force law, which has typically been used for impacts into three-dimensional granular systems composed of sand or glass beads, is also effective in describing impacts into two-dimensional systems of photoelastic disks. These disks have a range of stiffnesses that range from much softer than to comparable to sand and glass beads. The frictional properties of the 2D particles are comparable to those of sand or glass beads. Thus, many of the microscopic insights gained in the two-dimensional system should also be applicable to impacts in three-dimensional systems.
- 2) Even though this macroscopic force law is effective at capturing the trajectories on average, the instantaneous force is highly fluctuating in space and time. Physically, these fluctuations correspond to intermittent acoustic activity which occurs at the leading edge of the intruder as it moves. Thus, at the grain-scale, the intruder's energy is transferred to the granular material in a series of intermittent collisions with force-chain-like structures.
- 3) The deceleration is dominated by a velocity-squared drag term, and the strength of this collisional term,  $h(z)$ , shows significant dependence on intruder shape, even when holding mass and cross-sectional width constant. This effect can be understood with a collisional model which assumes that the origin of the drag force on the intruder is a series of random collisions with stationary clusters of grains. This model is extremely effective at capturing the drag coefficient over a wide range of intruder shapes, as well as capturing the dynamics of off-axis rotations. It is noteworthy that 'collisions' between the intruder and the granular bed, as observed directly in the photoelastic images, are typically normal to the intruder boundary. This effect is incorporated in the model by explicitly assuming that friction between the grains and the leading edge of the intruder can be ignored. The success of the model in quantitatively characterizing the drag forces on an intruder supports this assumption.
- 4) When the rate of force transmission is comparable to the intruder speed, the nature of the granular force response changes, and the Poncelet model breaks down. The strong force network (force chains) does not decay as the intruder advances, but rather, continues to grow at the front of the shock. Contacts in the compressed region have relatively large deformations. Since the particles are incompressible, these large deformations lead to the formation of additional contacts which further strengthen the compressed part of the sample which exists between the leading edge of the intruder and the shock front.

One obvious direction for future research would be to apply the collisional model to impacts in three dimensions. A number of 3D experiments with comparable impact and granular force propagation speeds also find  $v^2$  scaling for the dynamic part of the drag. An extension of the model to 3D is straight forward, and would involve extensions of Eqs. 6–9 to the leading surface of a 3D intruder. The fact that stresses from collisions can be determined within  $O(1)$  normalization suggests that it may be possible to use such an approach for applications, such as maximizing or minimizing the inertial drag or understanding the stability and dynamics of rotations of granular intruders as a function of intruder shape.

- 
- [1] William A. Allen, Earle B. Mayfield, and Harvey L. Morrison. Dynamics of a projectile penetrating sand. *Journal of Applied Physics*, 28(3):370–376, 1957.
  - [2] M.J. Forrestal and V.K. Luk. Penetration into soil targets. *International Journal of Impact Engineering*, 12(3):427 – 444, 1992.
  - [3] LS Tsimring and D Volfson. Modeling of impact cratering in granular media. *Powders and grains*, 2:1215–1223, 2005.
  - [4] Hiroaki Katsuragi and Douglas J. Durian. Unified force law for granular impact cratering. 3:420 – 423, 2007.
  - [5] Daniel I. Goldman and Paul Umbanhowar. Scaling and dynamics of sphere and disk impact into granular media. *Phys. Rev. E*, 77:021308, Feb 2008.

- [6] Paul Umbanhowar and Daniel I. Goldman. Granular impact and the critical packing state. *Phys. Rev. E*, 82:010301, Jul 2010.
- [7] Yuka Takehara, Sachika Fujimoto, and Ko Okumura. High-velocity drag friction in dense granular media. *EPL*, 92(4):44003, 2010.
- [8] Abram H. Clark, Lou Kondic, and Robert P. Behringer. Particle scale dynamics in granular impact. *Phys. Rev. Lett.*, 109:238302, Dec 2012.
- [9] A. H. Clark and R. P. Behringer. Granular impact model as an energy-depth relation. *EPL (Europhysics Letters)*, 101(6):64001, 2013.
- [10] Abram H. Clark, Alec J. Petersen, and Robert P. Behringer. Collisional model for granular impact dynamics. *Phys. Rev. E*, 89:012201, Jan 2014.
- [11] Massimo Pica Ciamarra, Antonio H. Lara, Andrew T. Lee, Daniel I. Goldman, Inna Vishik, and Harry L. Swinney. Dynamics of drag and force distributions for projectile impact in a granular medium. *Phys. Rev. Lett.*, 92:194301, May 2004.
- [12] M. A. Ambroso, C. R. Santore, A. R. Abate, and D. J. Durian. Penetration depth for shallow impact cratering. *Phys. Rev. E*, 71:051305, May 2005.
- [13] J. R. de Bruyn and A. M. Walsh. Penetration of spheres into loose granular media. *Canadian Journal of Physics*, 82(6):439–446, 2004.
- [14] Amanda M. Walsh, Kristi E. Holloway, Piotr Habdas, and John R. de Bruyn. Morphology and scaling of impact craters in granular media. *Phys. Rev. Lett.*, 91:104301, Sep 2003.
- [15] E. L. Nelson, H. Katsuragi, P. Mayor, and D. J. Durian. Projectile interactions in granular impact cratering. *Phys. Rev. Lett.*, 101:068001, Aug 2008.
- [16] K. A. Newhall and D. J. Durian. Projectile-shape dependence of impact craters in loose granular media. *Phys. Rev. E*, 68:060301, Dec 2003.
- [17] A. Seguin, Y. Bertho, P. Gondret, and J. Crassous. Sphere penetration by impact in a granular medium: A collisional process. *EPL (Europhysics Letters)*, 88(4):44002, 2009.
- [18] J. V. Poncelet. *Cours de Mécanique Industrielle*. Lithographie de Clouet, 1829.
- [19] Farhang Radjai, Michel Jean, Jean-Jacques Moreau, and Stéphane Roux. Force distributions in dense two-dimensional granular systems. *Phys. Rev. Lett.*, 77:274–277, Jul 1996.
- [20] Chu-heng Liu and Sidney R. Nagel. Sound in sand. *Phys. Rev. Lett.*, 68:2301–2304, Apr 1992.
- [21] Daniel Howell, R. Behringer, and Christian Veje. Stress fluctuations in a 2d granular couette experiment: A continuous transition. *Phys. Rev. Lett.*, 82:5241–5244, Jun 1999.
- [22] GW BAXTER, R LEONE, GA JOHNSON, and RP BEHRINGER. Time-dependence, scaling and pattern-formation for flowing sand. *EUROPEAN JOURNAL OF MECHANICS B-FLUIDS*, 10(2, S):181–186, 1991.
- [23] P. Dantu. Etude statistique des forces intergranulaires dans un milieu pulvérulent. *Gotechnique*, 18:50–55(5), 1968.
- [24] Takao Wakabayashi. Photo-elastic method for determination of stress in powdered mass. *Journal of the Physical Society of Japan*, 5(5):383–385, 1950.
- [25] A. Drescher and G. de Josselin de Jong. Photoelastic verification of a mechanical model for the flow of a granular material. *Journal of the Mechanics and Physics of Solids*, 20(5):337 – 340, 1972.
- [26] Abram H Clark, Alec J Petersen, Lou Kondic, and Robert P Behringer. Nonlinear force propagation during granular impact. *Physical review letters*, 114(14):144502, 2015.
- [27] Leopoldo R. Gómez, Ari M. Turner, Martin van Hecke, and Vincenzo Vitelli. Shocks near jamming. *Phys. Rev. Lett.*, 108:058001, Jan 2012.
- [28] L. Kondic, X. Fang, W. Losert, C. O’Hern, and R. Behringer. Microstructure evolution during impact on granular matter. *Phys. Rev. E*, 85:011305, Jan 2012.
- [29] Karen E. Daniels, Joyce E. Coppock, and Robert P. Behringer. Dynamics of meteor impacts. *Chaos: An Interdisciplinary Journal of Nonlinear Science*, 14(4):S4–S4, 2004.
- [30] C. Goldenberg and I. Goldhirsch. Friction enhances elasticity in granular solids. *Nature*, 435:188–191, 2005.
- [31] A.P.F. Atman, P. Brunet, J. Geng, G. Reydellet, P. Claudin, R.P. Behringer, and E. Clément. From the stress response function (back) to the sand pile dip. *The European Physical Journal E*, 17(1):93–100, 2005.
- [32] Junfei Geng, Emily Longhi, R. Behringer, and D. Howell. Memory in two-dimensional heap experiments. *Phys. Rev. E*, 64:060301, Nov 2001.
- [33] T. S. Majmudar and R. P. Behringer. Contact force measurements and stress-induced anisotropy in granular materials. *Nature*, 435:1079–1082, 2005.
- [34] T. Majmudar, M. Sperl, S. Luding, and R. P. Behringer. Jamming transition in granular systems. *Phys. Rev. Lett.*, 98:058001, Jan 2007.
- [35] J. Krim and R. P. Behringer. Friction, force chains, and falling fruit. *Physics Today*, 62:66–67, 2009.
- [36] Junfei Geng, D. Howell, E. Longhi, R. Behringer, G. Reydellet, L. Vanel, E. Clément, and S. Luding. Footprints in sand: The response of a granular material to local perturbations. *Phys. Rev. Lett.*, 87:035506, Jul 2001.
- [37] Jie Ren, Joshua A. Dijksman, and Robert P. Behringer. Reynolds pressure and relaxation in a sheared granular system. *Phys. Rev. Lett.*, 110:018302, Jan 2013.
- [38] Dapeng Bi, Jie Zhang, Bulbul Chakraborty, and R. P. Behringer. Jamming by shear. *Nature*, 480:355–358, 2011.
- [39] James Puckett and Karen Daniels. Equilibrating temperaturelike variables in jammed granular subsystems. *Phys. Rev. Lett.*, 110:058001, Jan 2013.
- [40] J. Zhang, T.S. Majmudar, A. Tordesillas, and R.P. Behringer. Statistical properties of a 2d granular material subjected

- to cyclic shear. *Granular Matter*, 12(2):159–172, 2010.
- [41] Junfei Geng, G. Reydellet, E. Clment, and R.P. Behringer. Greens function measurements of force transmission in 2d granular materials. *Physica D: Nonlinear Phenomena*, 182(34):274 – 303, 2003.
  - [42] Miguel Da Silva and Jean Rajchenbach. Stress transmission through a model system of cohesionless elastic grains. *Nature*, 406:708–710, 2000.
  - [43] Antoinette Tordesillas, Jie Zhang, and Robert Behringer. Buckling force chains in dense granular assemblies: physical and numerical experiments. *Geomechanics and Geoengineering*, 4(1):3–16, 2009.
  - [44] A. Drescher. An experimental investigation of flow rules for granular materials using optically sensitive glass particles. *Gotechnique*, 26:591–601(10), 1976.
  - [45] Brian Utter and R. Behringer. Experimental measures of affine and nonaffine deformation in granular shear. *Phys. Rev. Lett.*, 100:208302, May 2008.
  - [46] Danielle Bassett, Eli Owens, Karen Daniels, and Mason Porter. Influence of network topology on sound propagation in granular materials. *Phys. Rev. E*, 86:041306, Oct 2012.
  - [47] L. Kondic. Dynamics of spherical particles on a surface: Collision-induced sliding and other effects. *Phys. Rev. E*, 60:751, 1999.
  - [48] J. Schäfer, S. Dippel, and D. E. Wolf. Force schemes in simulations of granular materials. *J. Phys. I France*, 6:5, 1996.
  - [49] P. A. Cundall and O. D. L. Strack. A discrete numerical model for granular assemblies. *Géotechnique*, 29(1):47–65, 1979.
  - [50] L. Brendel and S. Dippel. Lasting contacts in molecular dynamics simulations. In H. J. Herrmann, J.-P. Hovi, and S. Luding, editors, *Physics of Dry Granular Media*, page 313, Dordrecht, 1998. Kluwer Academic Publishers.
  - [51] M. Lätzel. *From microscopic simulations towards a macroscopic description of granular media*. PhD thesis, Universität Stuttgart, Stuttgart, Germany, 2003.
  - [52] C. Goldenberg and I. Goldhirsch. Friction enhances elasticity in granular solids. *Nature*, 435:188, 2005.